Conductive Hybrid Cu-HHTP-TCNQ Metal–Organic Frameworks for Chemiresistive Sensing

Lars Lüder,* Agnes Gubicza, Michael Stiefel, Jan Overbeck, Davide Beretta, Amin Sadeghpour, Antonia Neels, Peter N. Nirmalraj, René M. Rossi, Claudio Toncelli, and Michel Calame*

Electrically conductive metal–organic frameworks (MOFs) and MOF-like coordination polymers are an emerging class of materials that combine good electrical charge transport with unique properties such as nanoporosity. The combination of different metal nodes and organic linkers allows tailoring MOFs to specific properties and applications in electronics, like selective chemiresistive sensing. The intrinsic crystallinity of MOFs, which usually promotes efficient charge transport, makes them also difficult to integrate into flexible systems, as crystalline MOFs are often brittle. The present study reports on a fast and reliable interfacial synthesis of conductive MOF films composed of two different organic ligands, 2,3,6,7,10,11-hexahydroxytriphenylene (HHTP) and 7,7,8,8-tetracyanoquinodimethane (TCNQ), lacking long-range periodic order while preserving good electrical conductivity of 0.033 S cm^{-1} at room temperature and chemiresistive response toward ambient changes. The hybrid nature of the discontinuous film is investigated multiparametrically by electron and atomic force microscopy as well as by Raman spectroscopy. This study demonstrates that including different types of MOFs is a good compromise between structural order and conductivity, thus making hybrid framework architectures to a promising active material for chemiresistive sensors without the need for high crystallinity.

1. Introduction

Metal–organic frameworks (MOFs) are a unique class of nanoporous materials composed of metal nodes, that are connected by organic linkers via coordination bonds to form a crystalline coordination network.[1] By assembling different building blocks, the physical and chemical characteristics can be tuned such as, for example, their inner surface area, which has already been demonstrated to reach up to 7310 m^2 g^{-1},[2] that is up to two orders of magnitude larger than that of other porous materials such as zeolithes and ceramic materials.[3] The selectivity of MOFs, means the ability to differentiate different target analytes, can also be adjusted by scaling the pore size[4] and a chemical functionalization,[5] offering a large versatility in structure and functionality.[6] These unique properties make MOFs a well-suited material for a wide range of applications such as gas storage and filtering,[7] catalysis,[8] sensing,[9] and water harvesting.[10]

Through careful choice of the organic and inorganic components, electrically conductive MOFs with good spatial and energetic overlap between orbitals of appropriate symmetry can be synthesized such that the charge carriers are delocalized over the framework structure.[11] To date, the most conductive MOFs have a planar structure with extended 2D π-conjugation due to their enhanced orbital coupling and charge delocalization,[12] reaching conductivity values of 2500 S cm^{-1}.[13] For instance, triphenylene-based MOFs show

L. Lüder, A. Gubicza, M. Stiefel, J. Overbeck, D. Beretta, P. N. Nirmalraj, M. Calame
Transport at Nanoscale Interfaces Laboratory
Empa
Swiss Federal Laboratories for Materials Science and Technology
Überlandstrasse 129, Dübendorf 8600, Switzerland
E-mail: lars.lueder@empa.ch; michel.calame@empa.ch

L. Lüder, J. Overbeck, M. Calame
Department of Physics and Swiss Nanoscience Institute
University of Basel
Klingelbergstrasse 82, Basel 4056, Switzerland

The ORCID identification number(s) for the author(s) of this article can be found under https://doi.org/10.1002/aelm.202100871.

[+]Present address: School of Food Science and Nutrition, University of Leeds, Leeds, LS2 9JT, UK

L. Lüder, A. Gubicza, A. Sadeghpour,[+] R. M. Rossi, C. Toncelli
Biomimetic Membranes and Textiles Laboratory
Empa
Swiss Federal Laboratories for Materials Science and Technology
Lerchenfeldstrasse 5, St. Gallen 9014, Switzerland

A. Sadeghpour, A. Neels
Center for X-ray Analytics
Empa
Swiss Federal Laboratories for Materials Science and Technology
Lerchenfeldstrasse 5, St. Gallen 9014, Switzerland

A. Neels
Department of Chemistry
University of Fribourg
Avenue de l'Europe 20, Fribourg 1700, Switzerland

R. M. Rossi
Department of Health Science and Technology
ETH Zürich
Zürich 8092, Switzerland

a planar graphene-like honeycomb lattice with open pores and exhibit high conductivity. Owing to their efficient 2D conjugation pathways, they reach room-temperature mobility of up to 220 cm^2 V^{-1} s^{-1},[14] The possibility to combine tunable material properties of MOFs with electrical charge transport has direct implications for energy storage,[15] electrocatalysis,[16] and chemiresistive sensing.[17]

Highly crystalline, defect-free MOFs are usually preferred to randomly arranged architectures for electrical charge transport, as their periodic structure leads to high mobility.[11c,18] Single crystals and well-grown MOF films of high structural order usually exhibit better conductivities than compressed powder, as has been demonstrated for nickel (II) hexaiminotriphenylene (Ni-HITP)[19] and copper (II) hexahydroxytriphenylene (Cu-HHTP).[20] Besides their enhanced conductivity, MOF films further provide an open structure and hence a high surface-to-volume ratio, which is beneficial or even essential for certain applications like gas sensing.[21]

However, MOF-like coordination polymers lacking long-range periodic order (also called amorphous MOFs) usually show higher mechanical robustness and isotropy compared to their crystalline equivalent[22] and could therefore be used in a broader range of applications, for example, for the incorporation into flexible devices.[23] One way of not sacrificing conductivity when synthesizing amorphous MOF architectures are hybrid MOF structures, that allow the formation of a heterogeneous structure with improved characteristics.[24]

In this paper, we present a fast and simple synthesis of a hybrid MOF film, composed of copper ions and two different organic ligands HHTP and TCNQ (hereon referred to as Cu-HHTP-TCNQ), that shows an average conductivity of 0.033 S cm^{-1} and a chemiresistive response toward ambient changes, despite its discontinuous architecture and its highly amorphous phase. Controlled growth of freestanding Cu-HHTP-TCNQ films is achieved by a biphasic, interfacial synthesis between two immiscible liquid phases.[25] The heterogeneous structure of the film and its morphology are examined by scanning electron microscopy (SEM) and atomic force microscopy (AFM), while its chemical composition and organic ligand distribution are analyzed by energy dispersive X-ray (EDX) and Raman spectroscopy. Electrical conductivity is measured in a four-wire configuration on a set of films deposited on glass substrates with prepatterned gold electrodes.

2. Results and Discussion

2.1. Synthesis

Cu-HHTP-TCNQ hybrid films were synthesized by a biphasic system of aqueous Cu(II) nitrate solution and ethyl acetate containing dissolved HHTP and TCNQ organic ligands (**Figure 1**, and Experimental Section for details). The coordination reaction between Cu^{2+}-ions and organic molecules started
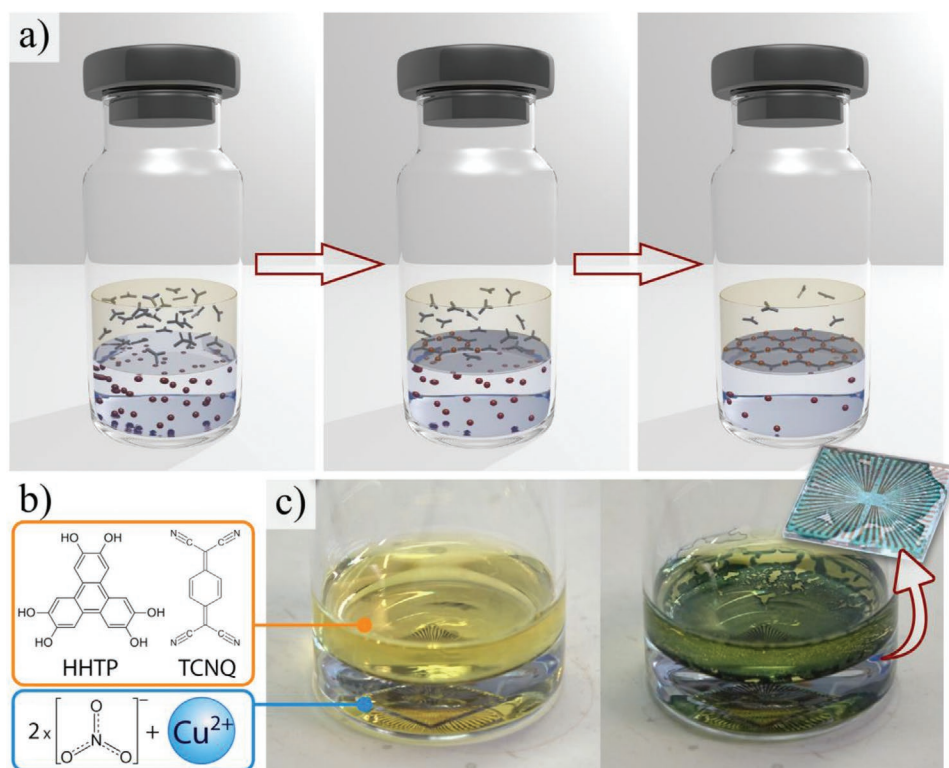
Figure 1. Synthesis of Cu-HHTP-TCNQ films. a) Schematic illustration of the formation process of thin coordination polymer films at the interface between bottom aqueous and top organic phase. Diffusion lets the separately dissolved metal ions and organic ligands meet at the interface, forming a coordinative bond. b) Molecular structure of organic ligands HHTP and TCNQ as well as copper nitrate as metal source. c) Photograph of interfacial film growth of Cu-HHTP-TCNQ at starting time (left) and after 15 min (right). The picture shows the fast growth of the dark film. Inset: Photograph of the film directly after deposition on a glass chip with gold electrodes.

immediately at the interface after merging the phases. The formation of a film was visible within 1 min at 0 °C, although still being nearly transparent owing to its small thickness. With a longer reaction time, the film became more opaque resulting in a clearly visible black film after 15 min, at the latest (Figure 1c). The growth of a continuous film was only initiated when both organic molecules were combined. The sole addition of HHTP led to the slow formation of nonconnected MOF powder after 1 h, known to consist of multiple nanosheets,[26] whereas TCNQ alone did not show any macroscopic reaction with copper ions. The lateral dimension of continuously grown Cu-HHTP-TCNQ film was defined by the reaction vial, encompassing an area of about 5 cm². When floating, the film is delicate and can break on light mechanical shocks. With increasing reaction time, mechanical stability seems to improve due to ongoing film growth because the floating film no longer broke so easily. For structural and electrical investigations of the film, it was transferred onto a substrate. Once the film is deposited, it remains stable and robust for analysis. Film deposition was realized by initially placing a substrate of choice on the bottom of the reaction vessel and carefully removing the liquid phases with a syringe after film growth, allowing the film to sink (Video S1, Supporting Information). For film characterization, glass substrates with prepatterned gold electrodes were used (Figure 1c, inset).

2.2. Surface Morphology

SEM images show the top view and the side view of the film, consisting of elongated filamentous features which are vertically aligned with respect to the film extent (**Figure 2**a,b). The arrangement of the filaments forms a continuous layer with gaps in between. Some parts of the film were folded, thus allowing a view of the bottom side. Crystalline entities of cubic appearance were found on the film's backside, which was facing the water phase during synthesis. The crystalline cubes were randomly oriented and distributed underneath the whole film and were already present after 10 min reaction time (Figure S1a, Supporting Information). At random locations, long crystalline rods were evident. Their origin lies within the cubic crystals at the bottom side, sticking out perpendicularly from the film by anisotropic growth in length (Figure S1c,d, Supporting Information).

Figure 2c–h shows AFM topographs recorded on films with varying reaction time ranging from 10 min where the thin film is just manageable, up to 80 min where no major change of the film can be observed anymore. Figure 2c displays a scanned area of a film with 10 min reaction time and shows a holey film, which was not completely closed yet. Increasing the reaction time to about 20 min results in a continuous film, which ends up in a rough topography due to ongoing growth in the liquid phase, as visible in Figure 2h. Formed elevations can probably be attributed to the cubic crystals in addition to the continuous film. Figure 2g (60 min reaction time) is displayed at a different scale because of limitations in large area scans with the AFM (explicitly shown in Figure S2, Supporting Information, showing high resolution images). Mean film thickness for each reaction time has been evaluated by line profile scans at the
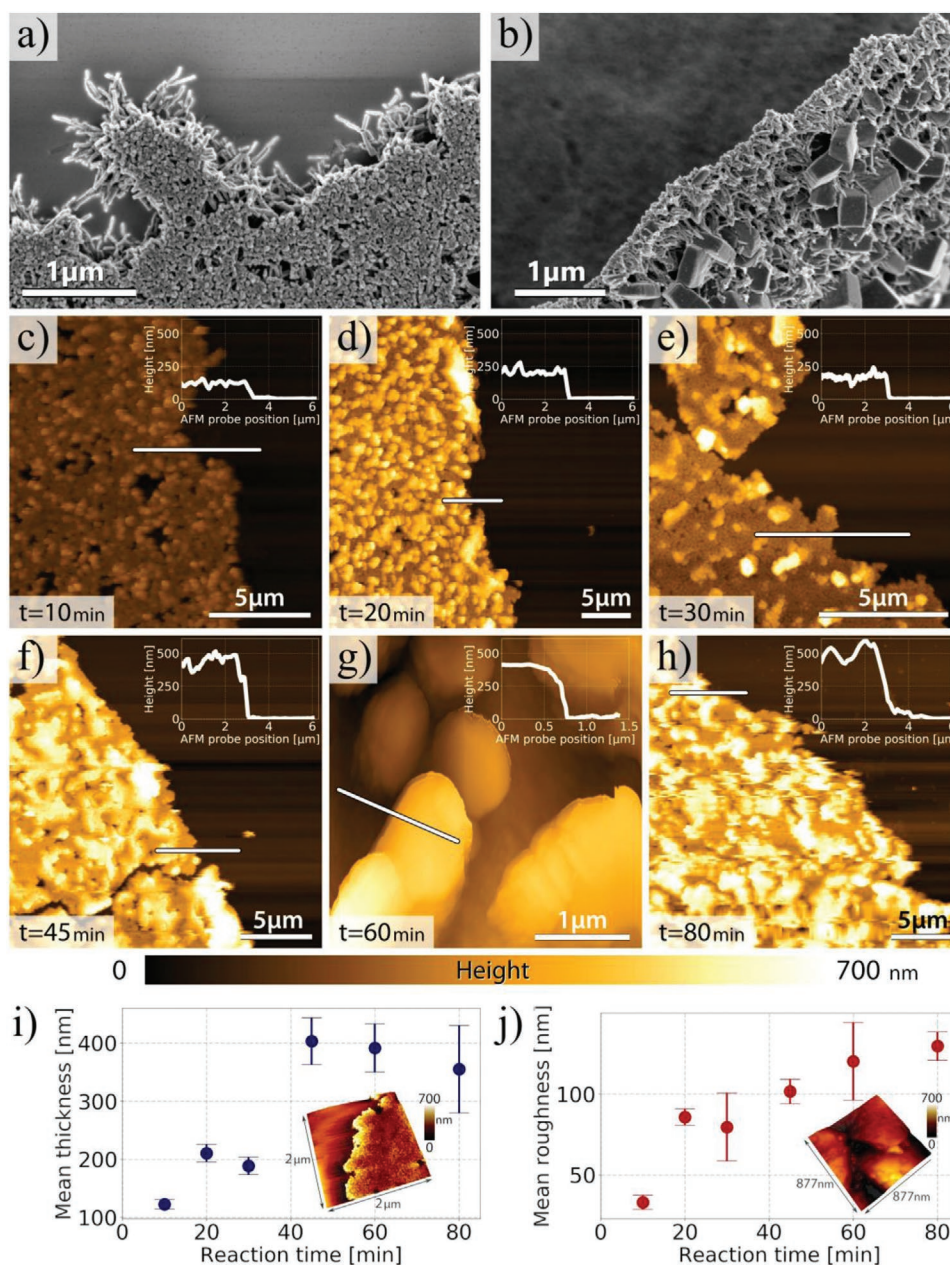
film border and correlated with the reaction time (Figure 2i and Figure S3, Supporting Information). It shows thicker films for longer reaction time, although the increase is not steady due to fluctuations in synthesis and variations of the heterogeneous material. Film growth is faster in the beginning due to easy diffusion of the reagents but slows down as the film thickens. Root mean square roughness of the films increases as well for longer reaction times as can be seen in Figure 2j. Small elevations that can be observed after 20 min at the latest develop over time into larger structures making the film rougher.

2.3. Elemental Distribution

In order to map the elemental distribution within the film, EDX spectroscopy was performed. The analysis of oxygen and nitrogen, in particular, allowed a differentiation between the organic ligands HHTP and TCNQ, since these elements occur separately in the respective molecular structures. In **Figure 3**a, a region of the film involving both, crystalline cubes and the continuous film, is imaged and analyzed by EDX. The measurement revealed the presence of oxygen and thus HHTP within the continuous part, but an absence of oxygen in the crystalline cubes. Cu-HHTP is known to form hexagonal-shaped filamentous rods[20b,27] similar to the features we found as main component of the continuous layer (Figure 2a), hence supporting the existence of HHTP. In contrast, nitrogen is distributed inversely and concentrated within the cubes, whereas the signal detected throughout the continuous part of the film is about half as strong. The nitrogen in the cubes can thus be attributed to TCNQ molecules as opposed to residual nitrate salts because of the lack of oxygen. However, the mapping of the elements and the identification of the ligand arrangement did not allow concluding whether the organic molecules were coordinated to copper or not, particularly since copper and carbon were distributed homogeneously over the area (Figure S4, Supporting Information).

2.4. Raman Spectroscopy

To identify the coordination between the organic linker and the copper ions, Raman spectroscopy was employed on the Cu-HHTP-TCNQ film. At different positions of the film, the acquired spectra show different intensities and Raman peaks, as can be seen in Figure 3b. The Raman spectrum of pure Cu-HHTP is known to have no distinct peaks,[28] possibly due to the fact that the molecule HHTP can exist in seven different oxidation states resulting in a blending of several vibrational modes.[29] Cu-TCNQ instead shows a clear Raman spectrum with mainly four pronounced vibrational modes. A clear agreement could be found between the blue spectrum in Figure 3b and the literature data for noncoordinated TCNQ.[30] When TCNQ molecules coordinate to copper ions, the C−CN stretching mode at the wavenumber 1450 cm^{-1} (Figure 3b, blue box) is shifted to 1380 cm^{-1} (Figure 3b, red box) as result of a charge transfer.[30a] Also, the C−N stretching mode at 2225 cm^{-1} shifts to lower frequencies and a new mode appears at 735 cm^{-1}. The red spectrum of Figure 3b is thus assigned

**ADVANCED
SCIENCE NEWS**

www.advancedsciencenews.com

**ADVANCED
ELECTRONIC
MATERIALS**

www.advelectronicmat.de

Figure 2. Characterization of Cu-HHTP-TCNQ film morphology. a,b) Scanning electron microscopy (SEM) images of Cu-HHTP-TCNQ thin films with 60 min reaction time from the top (a) and from the bottom (angled) (b) showing filamentous features substantially aligned in parallel and cubic crystals on the film downside. c–h) Atomic force microscopy (AFM) measured the topography of Cu-HHTP-TCNQ films from 10 min (c) to 80 min (h) reaction time. Profile line scans were performed on all scanned areas to evaluate film thickness. Selected profiles are shown as inset. i) Mean film thickness over reaction time, evaluated from profile scans at five different edge positions. Film thickness increases for longer reaction times. Inset: 3D topography of selected film border for better overview. j) Root mean square roughness over reaction time, evaluated at five film sections. Film roughness increases for longer reaction times. Inset: 3D topography of selected film section for better overview.

to TCNQ coordinated to copper ions. The green curve does not display any peak corresponding to TCNQ but some weak signal at the positions where Cu-HHTP is known to be Raman active.[28]

A 2D Raman scan was performed on a region with cubic crystals in the continuous film as identified with optical microscopy in Figure 3c. For better resolution, SEM images were taken at the locations of the Raman scan and overlaid in order

to map the peak signal and hence the ligand distribution. In Figure 3d, the 2D intensity plot at 1380 ± 30 cm^{-1} is shown representing the presence of TCNQ molecules coordinated to copper ions. The signal is strong at locations with cubic crystals, which is a clear indication of a high concentration of coordinated TCNQ. This finding is consistent with the enrichment of nitrogen within the cubes as known from EDX spectroscopy (Figure 3a and Figure S4, Supporting Information). The
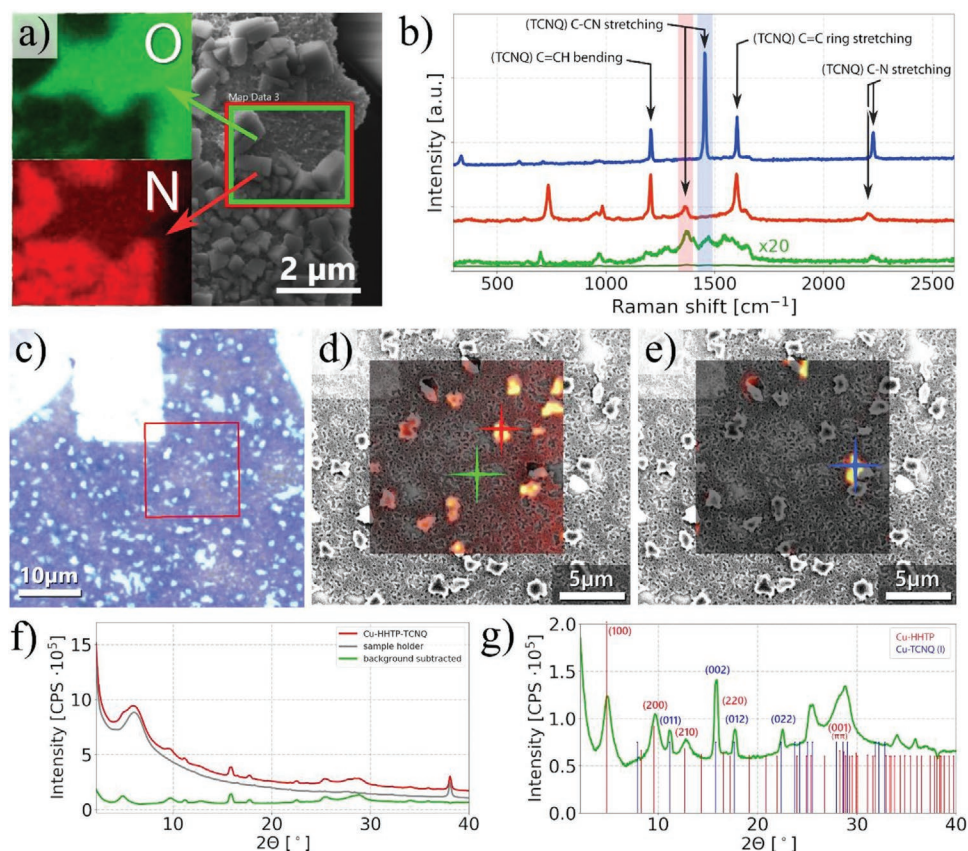
Figure 3. Elemental analysis of synthesized Cu-HHTP-TCNQ films. a) Energy dispersive X-ray (EDX) spectroscopy map of Cu-HHTP-TCNQ. The elemental distribution of oxygen and nitrogen reveals the ligand arrangement within the film structure and confirms an accumulation of nitrogen in the cubic crystals, whereas oxygen is entirely present in the filamentary features. b) Raman spectra at three different positions on the Cu-HHTP-TCNQ film. Noncoordinated TCNQ molecules have a prominent peak at 1450 cm^{-1} (blue box) based on the C—CN stretching mode, which shifts to 1380 cm^{-1} (red box) when coordinating to copper ions. The spectra are plotted with an offset for clarity and the green spectrum is also displayed with a multiplication factor of 20. c) Optical microscopy image of Cu-HHTP-TCNQ film after 30 min reaction time. The bright signal on the top is a gold marker that allows alignment of SEM and Raman images. The red square indicates the area of the Raman scan. d,e) Overlay of SEM images and 2D Raman intensity plots at the wavenumbers 1380 ± 30 cm^{-1} (d) and 1450 ± 30 cm^{-1} (e). The Raman signal distribution at 1380 cm^{-1} affirms the accumulation of coordinated TCNQ molecules in the cubic crystals, whereas the distribution at 1450 cm^{-1} shows that noncoordinated TCNQ is present only in a few isolated spots. The colored crosses indicate the position of the single Raman spectra shown in (b). f) XRD pattern of Cu-HHTP-TCNQ, which is measured as powder in reflection mode for 60 h. A background measurement (sample holder without sample) was carried out with same parameters and background subtraction from the Cu-HHTP-TCNQ signal was performed. g) Zoom-in for the background subtracted pattern. Peaks representing the crystalline part can be seen on a background, which indicates the amorphous quantity. The lines show the position of known reflections from Cu-HHTP (red) and Cu-TCNQ (I) (blue).

2D intensity plot at the wavenumber 1450 ± 30 cm^{-1} does not show increased signal at locations with cubic crystals and thus excludes the accumulation of noncoordinated TCNQ molecules in the cubes (Figure 3e). With the exception of a few random locations, the displayed part did not show a high Raman intensity at 1450 cm^{-1}, suggesting that there is no or very little noncoordinated TCNQ in this area.

On a larger scale, optical microscopy showed distinct regions of the Cu-HHTP-TCNQ film with different optical appearance. The investigation of their border with SEM revealed an unequal density of the crystalline cubes in the two regions (Figure S5, Supporting Information). On the parts where the crystalline cubes were concentrated, the continuous film was more disrupted and less connected. Raman scans showed a stronger signal at 1380 cm^{-1} on one side of the border, indicating coordinated TCNQ in form of cubes, whereas the signal at 1450 cm^{-1}

is predominant in the other region, indicating noncoordinated TCNQ molecules (Figure S5e,f, Supporting Information). A similar investigation for mapping of HHTP via Raman spectroscopy was not possible because of the weak signal-to-noise ratio and the overlapping strong signal from TCNQ.

2.5. X-Ray Diffraction

To get more insight into the structure of Cu-HHTP-TCNQ, X-ray diffraction (XRD) was performed, which revealed diffraction peaks at known positions from crystalline Cu-HHTP[20a,26] as for example the reflections (100) and (200) (corresponding to the 2D polymer in-plane long-range ordering) and (001) (corresponding to the π–π-stacking) (Figure 3f,g). Also, Cu-TCNQ (phase I) can be clearly confirmed by indexing the reflections (011), (002),

ADVANCED
SCIENCE NEWS
www.advancedsciencenews.com

ADVANCED
ELECTRONIC
MATERIALS
www.advelectronicmat.de

(012), and (022) among others.[30a,31] TCNQ is known to form two different phases with copper ions with distinct crystal structures (phases I and II).[30c,31] Even though the unit cell parameters are known from the CCDC database for phase I, a quantification of the phase would require atomic coordinates, which are not available to the best of our knowledge. In contrast, no features of phase II were detected in the XRD pattern.

Although the results indicate the presence of coordinated HHTP and TCNQ ligands forming two crystalline phases within the film, the XRD signal is accompanied by a strong background signal representing a high amorphous quantity of the sample. The X-ray characterization of amorphous MOFs is more challenging due to the absence of Bragg peaks in diffraction patterns.[22] A background measurement has been carried out to exclude weak peaks from the sample environment. The combination of two different ligands may disrupt the order of the film resulting in a lower crystalline structure and less long-range order. The high amorphous quantity could be also partially reasoned by the occurrence of some noncovalent architectures, based on the π–π-interactions between the aromatic rings of the ligands, forming stable organic frameworks as documented in literature.[32] A crystallite size estimation for selected crystal orientations using the Scherrer formula gave a crystallite size of 12 nm for Cu-HHTP ((200)-reflection) and 24 nm for

Cu-TCNQ (I) ((002)-reflection). The XRD pattern of the Cu-HHTP-TCNQ didn't change when measured after washing and drying compared to the signal measured directly after synthesis, which is an indication for a stable and reproducible structure. The examination of the film with transmission electron microscopy (TEM) and corresponding selected area electron diffraction (SAED) also shows the picture of largely amorphous films, since for the most part no diffraction peaks could be observed. SAED signals are seen in some regions, but these occur randomly and cannot be assigned to the crystalline cubes or the continuous film (Figure S6, Supporting Information).

Presence of porosity in Cu-HHTP-TCNQ films was assessed by the grazing-incidence-small-angle X-ray scattering (GI-SAXS). The strong scattering intensities recorded in the range of 0.1–1 nm^{-1} (roughly five times stronger than the one of the silicon substrate as the reference) indicated the presence of pores within the sample in nanoscale (Figure S7, Supporting Information).

2.6. Electrical Properties

To investigate the electrical properties of the synthesized Cu-HHTP-TCNQ films, we transferred the MOFs on glass chips with prepatterned gold electrodes (**Figure** 4a, and
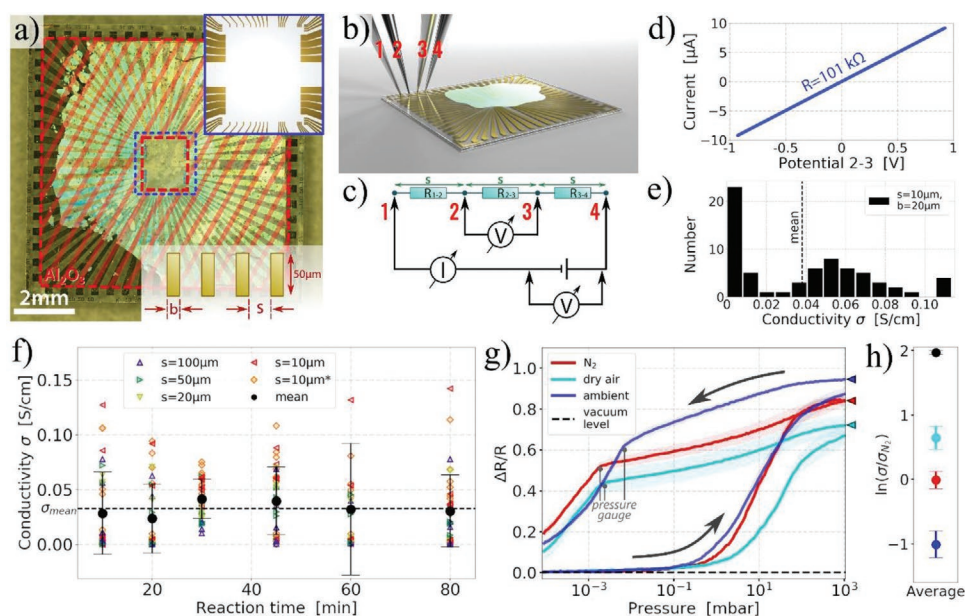
Figure 4. Electrical charge transport measurements. a) Dark-field microscopy image of chip coated with Cu-HHTP-TCNQ film. The red dashed area indicates the insulating Al_2O_3 layer between chip and film preventing short circuits. Inset top: Illustrative zoom-in into inner contacts with different dimensions. Inset bottom: Schematic of inner contact geometries. The ratio between contact width, b, and distance, s, is changing. b) Geometry of the prepatterned glass chip with gold electrodes contacted by needle probe actuators in a four-point probe. Deposited Cu-HHTP-TCNQ film is colored in cyan. c) Simplified electrical circuit of configuration. d) Typical I–V-curve of Cu-HHTP-TCNQ film (in vacuum), synthesized at 0 °C for 45 min. Linear slope indicates Ohmic behavior (sweeping rate = 12 V s^{-1}). e) Histogram of film conductivities for one contact geometry ($s = 10$ μm, $b = 20$ μm). f) Conductivity values from transport measurements of Cu-HHTP-TCNQ films with varying reaction times at different contact geometries (sweeping rate = 12 V s^{-1}). Contact width $b = 10$ μm for all data depicted as triangles and $b = 20$ μm for data depicted as diamonds, also marked with *. Black circles display the mean values and error bars indicate standard deviations. One single outlier at $\sigma = 0.306$ S cm^{-1} (time = 60 min, $s = 20$ μm) is not shown for better visibility. The dashed line represents the average conductivity. g) Relative response (change in film resistance) versus pressure during venting the vacuum chamber with nitrogen, dry air, and ambient air with a relative humidity of 41% (average of $N = 3$, colored area displays standard deviation; measured Cu-HHTP-TCNQ film was the same as shown in [d]; contact spacing $s = 20$ μm). Arrows indicate the cycling direction, starting at vacuum level. Triangles point to the saturation value. h) Normalized average film conductivities when exposed to different atmospheres. σ_{N_2} represents film conductivity in a nitrogen atmosphere.

**ADVANCED
SCIENCE NEWS**

www.advancedsciencenews.com

**ADVANCED
ELECTRONIC
MATERIALS**

www.advelectronicmat.de

Experimental Section for details on the fabrication). Each chip included N contacts, fabricated in the center and connected to large pads on the outer edges by gold leads. To prevent short circuits between adjacent devices, the leads were covered by an insulating Al_2O_3 layer. Different geometries of the contacts (varying contact distances, s, from 10 to 100 μm) were realized for evaluating possible variations in contact performance. The electrical conductance was measured in a collinear four-point probe geometry as displayed in Figure 4b. A voltage was applied to the two outer contacts and swept linearly over time driving a current flowing through the sample, whereas the inner contacts tapped the voltage drop. Figure 4d shows the IV traces of a representative sample. The film displays an Ohmic behavior, with a resistance of 100.8 kΩ in vacuum at room temperature. In a four-point probe geometry, the film resistivity ρ can be derived from the general formula $\rho = \dfrac{U}{I}\Gamma$ where U and I are the voltage in volt and current in ampere, respectively, and Γ is a geometrical correction factor of length dimension, taking into account the sample thickness. For thin films ($\frac{t}{s} \leq 0.5$) of infinite size ($d \geq 40\ s$) with thickness t, contact spacing s and limiting contour diameter d, the film resistivity is $\rho = \dfrac{\pi}{ln(2)}\dfrac{U}{I}t$.[33]

206 contacts were analyzed for films with reaction times ranging from 10 min up to 80 min. Conductivity values $\sigma = \dfrac{1}{\rho}$ were evaluated by using the average film thicknesses obtained by AFM measurements. Since the synthesis method leads to a variation in film thickness on the length scale of the measured inter-electrode area and since the film consists of different phases with individual conducting properties (Cu-HHTP, Cu-TCNQ (I)), the value does not provide an intrinsic material property but an average quantity. In Figure 4f, the conductivity values are plotted against reaction time for contact geometries which differ in their contact spacing s from 10 to 100 μm. At least five measurements were performed on each contact geometry for different reaction times in order to validate the reproducibility. The mean conductivity amounts to $\sigma_{mean} = 0.033 \pm 0.006$ S cm^{-1} and is comparable with known Cu-HHTP values from literature (Cu-HHTP pressed pellets: 0.045 S cm^{-1}).[20a] Temperature-dependent measurements demonstrate that the electrical conductivity of Cu-HHTP-TCNQ around room temperature can be described by a thermally activated process with an activation energy of about 0.142 eV (Figure S8, Supporting Information). We attribute the scattering of the data points in Figure 4f to different regions as revealed by our optical analysis as well as film-to-film variations, probably caused by physical deposition issues or fluctuations in the synthesis of the different batches. Similar findings are known from the literature.[34]

2.7. Chemiresistive Response

We demonstrated the basic chemiresistive response of the synthesized MOF films as proof of principle by flushing the vacuum measurement chamber with nitrogen, dry air, and ambient air with a relative humidity of 41% during monitoring

the film resistance and pressure over time. Figure 4g displays the relative changes in resistance with respect to the vacuum level when the different gases are applied to a Cu-HHTP-TCNQ film, synthesized at 0 °C for 45 min. Starting from low pressure, resistances start to rise from about 10^{-1} mbar and go into saturation when atmospheric pressure is reached, indicated by small triangles. Delayed resistance changes at the same atmospheric pressure result in small discrepancies (Figure S9, Supporting Information). All curves displayed a hysteresis after pumping down, which could be explained by the higher energy needed to remove the adsorbed gas molecules from the pores and surfaces. The kink between 10^{-2} and 10^{-3} mbar is a measurement artifact originated from an ignition lag between the Pirani and cold-cathode element of the pressure gauge. Ambient air shows the strongest increase in film resistance, followed by pure nitrogen and dry air. One suggestion for the strong response toward ambient air is the interaction with water molecules owing to their polar character.[17a] The difference in response between nitrogen and dry air points toward a chemiresistive effect beyond that of water that should be investigated in future studies.

Normalized average film conductivities (normalized to σ_{N_2} which represents the film conductivity in a nitrogen atmosphere) under the different atmospheres were evaluated in order to put the chemiresistive response of the Cu-HHTP-TCNQ film in relation to known results (Figure 4h). Previous work showed comparable chemiresistive responses of Cu-HHTP films toward ambient changes,[35] thus demonstrating the potential applicability of Cu-HHTP-TCNQ films as a chemiresistive material, and paving the way for future work toward the development of HHTP-TCNQ-based chemiresistive sensors.

3. Conclusions

In summary, we demonstrated the fast synthesis and physical deposition of free-standing hybrid Cu-HHTP-TCNQ films by an interfacial assembly approach. Our process has the advantage of yielding a uniform film thickness controlled by the reaction time and is sufficiently robust to allow film deposition onto a variety of substrates. The hybrid film is shown to be composed of filaments and cubic crystals by coordination of Cu^{2+}-ions to the individual organic molecules. The influence of reaction time on the thickness and surface roughness is clarified using high-resolution AFM measurements. The multiparametric analysis further illustrates the hybrid architecture and the separation of the phases Cu-HHTP and Cu-TCNQ (I) embedded in a film structure coming along with low structural order. Electrical characterization of the Cu-HHTP-TCNQ films reveals an average conductivity of 0.033 S cm^{-1} and chemiresistive response toward ambient environmental shifts. The outcomes of this work demonstrate a potentially good applicability of less ordered MOF structures as chemiresistive materials and provide an insight into the potential of emerging hybrid MOF architectures.

4. Experimental Section

Materials: Cu(NO$_3$)$_2$·xH$_2$O (CAS: 13778-31-9), TCNQ (7,7,8,8-Tetracyanoquinodimethane, CAS: 1518-16-7) and ethyl acetate

(CAS: 141-78-6) were purchased from Merck (Sigma Aldrich). HTTP (Triphenylene-2,3,6,7,10,11-hexaol; 98%, CAS: 865836-87-9) was purchased from abcr swiss AG. All solvents were degassed with argon before use.

Synthesis of Cu-HHTP-TCNQ Films: The MOF thin films were synthesized in small glass vials (V = 15 mL, ND = 22) sealed and filled with argon and placed in an ice bath in order to keep reaction temperature at $T = 0$ °C. 2 mL of aqueous Cu(II) nitrate solution (10 mM) were added to the vial, followed by 1 mL of HHTP dissolved in ethyl acetate (0.4 mM) forming a water–organic solvent interface. The MOF film formation directly started at the interface when adding 1 mL of TCNQ dissolved in ethyl acetate (4 mM) and was visible by eye.

For transfer of the MOF film, a substrate of choice was placed at the bottom of the vial before the reaction started. The used substrates were treated with air plasma for 5 min to remove any resist residues and to improve wetting properties. The synthesis reaction was stopped after the desired time by carefully removing all the liquid with a syringe and thus sinking the thin film down onto the substrate. After drying the film in the air, the deposited film was washed in acetone and isopropyl alcohol, followed by second drying in the air.

Fabrication of Chips with Prepatterned Electrodes: For patterning the electrodes of the chip, a mask for UV lithography was fabricated by direct laser writing. A fused silica wafer (4 inches, 500 µm thickness, MicroChemicals GmbH) was spin-coated with AZ2020nlof resist (4000 rpm, 40 s) and soft-baked for 1 min at 110 °C. The pattern was exposed at a dose of 60 mJ cm^{-2}, followed by a postexposure bake for 1 min at 110 °C and development in AZ726mif for 30 s. Titanium (5 nm) and gold (50 nm) were then evaporated and the resist was removed by lift-off process in dimethylsulfoxide for 1 h at 110 °C. Al$_2$O$_3$ (50 nm) was deposited using plasma-enhanced atomic layer deposition in order to form an insulating passivation layer. To form the MOF contact and probe pad openings the wafer was again spin-coated with AZ1505 at 4000 rpm for 40 s and soft-baked at 110 °C for 1 min. The patterns for contact and probe pads were then exposed at a dose of 20 mJ cm^{-2} and developed for 20 s in AZ400k:H2O 1:4. The pattern transfer into the oxide was carried out by means of wet chemical etching in phosphoric acid (85%) at 55 °C for 105 s. For dicing, the wafer was again spin-coated with the same positive resist (AZ1505) at 1500 rpm for 40 s and soft-baked at 110 °C for 1 min.

Atomic Force Microscopy Characterization: For the AFM measurements, a Bruker Dimension Icon AFM equipped with a hybrid scanner was used. The AFM probe was a SCANASYST-AIR cantilever (BRUKER) with a tip apex radius of 2 nm and the AFM scan was performed in tapping mode under standard laboratory conditions without temperature or environmental control (resonant frequency: 70 kHz; force constant: 0.4 N m^{-1}). The cantilever was cleaned with acetone and isopropanol and dried with nitrogen before usage. The recorded AFM scan data was evaluated and leveled by Gwyddion software (version 2.55).

Raman Spectroscopy: Raman spectra and corresponding optical images were acquired in ambient conditions using a WITec Alpha 300R confocal Raman microscope with a 100× objective (Zeiss EC Epiplan-Neofluar Dic, NA = 0.9) and a 300 mm lens-based spectrometer (grating: 600 g mm^{-1}) equipped with a TE-cooled charge-coupled device (Andor Newton). The linearly polarized laser excitation had the wavelength $\lambda_{exc} = 488$ nm and a power of $P = 0.3$ mW measured before the objective. 2D Raman maps of size 15 µm × 15 µm were acquired in backscattering geometry with an integration time of 1.6 s and a resolution of 3 pixels per µm. Single spectra were extracted from the area scans at representative positions and were displayed after polynomial background subtraction.

Electrical Transport Measurements: For the electrical conductance measurements, a custom setup was used to monitor the current–voltage characteristics of the sample. The voltage was applied using a data acquisition card from National Instruments (model: NI 6289) and swept linearly over time (amplitude = 3 V, sweeping rate = 12 V s^{-1}). The current was monitored using a current amplifier (SP895/SP895a, University of Basel) and the measurement was controlled via a LabView program. *I–V*-measurements of electrically nonconducting devices (below the threshold of 1 nS) originated by, for example, lack of physical contact or film imperfections were not considered for the further data evaluation.

The authors performed the pressure-dependent measurements (PXR 36X vacuum gauge from Pfeiffer Vacuum) using nitrogen (N$_2$ 5.0) and compressed air (pressurized air, Sauerstoffwerk Lenzburg AG), taking care to flush the lines with the respective gas.

Temperature-Dependent Electrical Measurements: The temperature-dependent electrical conductivity was measured in a variable temperature cryostat (Lakeshore ST-500) using a Keithley 236 SMU controlled via Python pyvisa. The electrical conductivity was measured in a four-point collinear configuration. *I–V*-lines were taken by forcing a maximum current of 9 nA, with a sweeping rate of 0.1 nA s^{-1}. The temperature was controlled by a Lakeshore 336 temperature controller with resolution in the mK-range.

X-Ray Diffraction: Repeated synthesis of Cu-HHTP-TCNQ films (standard interfacial procedure at $T = 0$ °C for 45 min) and subsequent merging led to a larger amount of powder for investigations by XRD. The sample was measured on a PANALYTICAL X'pert Powder instrument equipped with an imaging plate using a CuKα X-ray source with $\lambda = 1.5406$ Å for 60 h. Data acquisition was conducted in reflection mode.

Crystallite sizes could be derived from the full width at half maximum of single indexed (nonoverlapping) reflections for selected crystal directions using the Scherrer equation ((200) for Cu-HHTP; (002) for Cu-TCNQ). The crystal elongation in the (100) and the (001) crystallographic direction for Cu-HHTP and Cu-TCNQ was calculated. For all other crystallographic directions, no single indexed lines were found. The instrumental peak broadening resolution was taken from the (111) reflection of the reference polycrystalline silicon.

For the analysis of the stability of Cu-HHTP-TCNQ toward washing and drying, thin films were synthesized (standard interfacial procedure at $T = 0$ °C for 45 min) and then collected by a loop sample holder. Diffraction measurements were performed directly after synthesis by STOE IPDS II instrument equipped with an imaging plate using MoKα X-ray source ($\lambda = 0.7107$ Å) and compared with the data obtained from washed and dried samples. Data acquisition was conducted in transmission mode while the sample was rotating (beam diameter = 0.5 mm).

Transmission Electron Microscopy: MOF films were synthesized for TEM imaging by the standard interfacial procedure at $T = 0$ °C for 40 min and then fished onto a copper grid (G2400C, square 400 mesh, Cu 3.05 mm diameter). TEM images were taken using JEOL 2200FS equipment with energy of 200 keV and 0.3 s exposure time. SAED signals were recorded at corresponding positions with camera lengths of 100 and 60 cm, respectively, with a SAED aperture introduced in order to define the sample region.

Grazing-Incidence Small-Angle X-Ray Scattering: MOF films were synthesized for GI-SAXS measurements by the standard interfacial procedure at $T = 0$ °C for 40 min and then deposited onto a silicon wafer substrate (orientation (100), thickness of 500 µm with a 285 nm native SiO$_2$ layer on top). Silicon substrates were rinsed with deionized water and treated with air plasma for 5 min before being placed at the bottom of the vial. The GISAXS experiments were performed using a Nanostar X-ray Scattering equipment (Bruker AXS GmbH, Germany) equipped with 2D Xe-based gaseous avalanche detector (VANTEC-2000 detector) of ×2048 pixels and the pixel size of 68 × 68 µm. A microfocused X-ray CuKα (wavelength $\lambda = 0.154$ nm) source with Montel optics and two pinhole collimation systems provided a point-focused beam diameter of around 500 µm. The setup was calibrated for the sample to detector distance using a standard silver behenate powder sample. This setup benefits from a GISAXS stage which allows sample movements in all directions with a resolution of 0.01 mm as well as rotations around all sample axes with an angular resolution of 0.0001°. The incident grazing angles were tuned between 0.15° and 0.3°. All experiments were performed in vacuum (≈0.01 mbar).

Supporting Information

Supporting Information is available from the Wiley Online Library or from the author.

Conflict of Interest

The authors declare no conflict of interest.

Author Contributions

L.L., A.G., R.M.R., C.T., and M.C. conceived and designed the study. L.L. performed the chemical synthesis, electrical measurements, and Raman measurements. A.G. built the electrical measurement setup, designed, and fabricated the glass chips with gold electrodes together with M.S. M.S. also conducted the SEM and EDX elemental analysis. J.O. and A.G. also carried out Raman measurements. P.N.N. performed the AFM measurements and data analysis. D.B. supervised the temperature-dependent electrical measurements. A.S. characterized the samples with GISAXS. A.N. carried out the XRD experiments and analyzed the diffraction data. L.L., P.N.N., M.C., and R.M.R. wrote the manuscript. All authors commented on the manuscript and provided critical feedback.

Data Availability Statement

The data that support the findings of this study are available from the corresponding author upon reasonable request.

[1] a) B. F. Hoskins, R. Robson, *J. Am. Chem. Soc.* **1990**, *112*, 1546; b) O. M. Yaghi, H. Li, *J. Am. Chem. Soc.* **1995**, *117*, 10401.

[2] Z. Chen, P. Li, R. Anderson, X. Wang, X. Zhang, L. Robison, L. R. Redfern, S. Moribe, T. Islamoglu, D. A. Gómez-Gualdró, T. Yildirim, J. F. Stoddar, O. K. Farha, *Science* **2020**, *368*, 297.

[3] a) Y. Tao, H. Kanoh, L. Abrams, K. Kaneko, *Chem. Rev.* **2006**, *106*, 896; b) R. Pullar, R. M. Novais, A. P. F. Caetano, M. A. Barreiros, S. Abanades, F. A. C. Oliveira, *Front. Chem.* **2019**, *7*, 601.

[4] M. Eddaoudi, J. Kim, N. Rosi, D. Vodak, J. Wachter, M. O'Keeffe, O. M. Yaghi, *Science* **2002**, *295*, 469.

[5] a) Y. Zhang, S. Yuan, X. Feng, H. Li, J. Zhou, B. Wang, *J. Am. Chem. Soc.* **2016**, *138*, 5785; b) Y. Peng, H. Huang, Y. Zhang, C. Kang, S. Chen, L. Song, D. Liu, C. Zhong, *Nat. Commun.* **2018**, *9*, 187.

[6] a) R. Banerjee, A. Phan, B. Wang, C. Knobler, H. Furukawa, M. O'Keeffe, O. M. Yaghi, *Science* **2008**, *319*, 939; b) M. Y. Masoomi, A. Morsali, A. Dhakshinamoorthy, H. Garcia, *Angew. Chem., Int. Ed.* **2019**, *58*, 15188.

[7] a) D. Sun, S. Ma, Y. Ke, D. J. Collins, H.-C. Zhou, *J. Am. Chem. Soc.* **2006**, *128*, 3896; b) K. Zhang, Q. Huo, Y.-Y. Zhou, H.-H. Wang, G.-P. Li, Y.-W. Wang, Y.-Y. Wang, *ACS Appl. Mater. Interfaces* **2019**, *11*, 17368; c) U. Mueller, M. M. Schubert, F. Teich, H. Puetter, K. Schierle-Arnd, J. Pastré, *J. Mater. Chem.* **2006**, *16*, 626.

[8] a) S.-Y. Moon, E. Proussaloglou, G. W. Peterson, J. B. DeCoste, M. G. Hall, A. J. Howarth, J. T. Hupp, O. K. Farha, *Chem. - Eur. J.* **2016**, *22*, 14864; b) K. Ma, T. Islamoglu, Z. Chen, P. Li, M. C. Wasson, Y. Chen, Y. Wang, G. W. Peterson, J. H. Xin, O. K. Farha, *J. Am. Chem. Soc.* **2019**, *141*, 15626; c) J. Lee, O. K. Farha, J. Roberts, K. A. Scheidt, S. T. Nguyen, J. T. Hupp, *Chem. Soc. Rev.* **2009**, *38*, 1450.

[9] a) F.-Y. Yi, D. Chen, M.-K. Wu, L. Han, H.-L. Jiang, *ChemPlusChem* **2016**, *81*, 675; b) X.-Y. Dong, Y. Si, J.-S. Yang, C. Zhang, Z. Han, P. Luo, Z.-Y. Wang, S.-Q. Zang, T. C. W. Mak, *Nat. Commun.* **2020**, *11*, 3678; c) M. R. Tchalala, P. M. Bhatt, K. N. Chappanda, S. R. Tavares, K. Adil, Y. Belmabkhout, A. Shkurenko, A. Cadiau, N. Heymans, G. D. Weireld, G. Maurin, K. N. Salama, M. Eddaoudi, *Nat. Commun.* **2019**, *10*, 1328.

[10] a) H. Kim, S. Yang, S. R. Rao, S. Narayanan, E. A. Kapustin, H. Furukawa, A. S. Umans, O. M. Yaghi, E. N. Wang, *Science* **2017**, *356*, 430; b) N. Hanikel, M. S. Prévot, F. Fathieh, E. A. Kapustin, H. Lyu, H. Wang, N. J. Diercks, T. G. Glover, O. M. Yaghi, *ACS Cent. Sci.* **2019**, *5*, 1699.

[11] a) Y. Kobayashi, B. Jacobs, M. D. Allendorf, J. R. Long, *Chem. Mater.* **2010**, *22*, 4120; b) L. S. Xie, G. Skorupskii, M. Dincă, *Chem. Rev.* **2020**, *120*, 8536; c) L. Sun, M. G. Campbell, M. Dincă, *Angew. Chem., Int. Ed.* **2016**, *55*, 3566; d) C. F. Leong, P. M. Usov, D. M. D'Alessandro, *MRS Bull.* **2016**, *41*, 858; e) M. Ko, L. Mendecki, K. A. Mirica, *Chem. Commun.* **2018**, *54*, 7873.

[12] a) R. Gutzler, D. F. Perepichka, *J. Am. Chem. Soc.* **2013**, *135*, 16585; b) D. Sheberla, J. C. Bachman, J. S. Elias, C.-J. Sun, Y. Shao-Horn, M. Dincă, *Nat. Mater.* **2017**, *16*, 220.

[13] Z. Jin, J. Yan, X. Huang, W. Xu, S. Yang, D. Zhu, J. Wang, *Nano Energy* **2017**, *40*, 376.

[14] R. Dong, P. Han, H. Arora, M. Ballabio, M. Karakus, Z. Zhang, C. Shekhar, P. Adler, P. S. Petkov, A. Erbe, S. C. B. Mannsfeld, C. Felser, C. Felser, T. Heine, M. Bonn, X. Feng, E. Cánovas, *Nat. Mater.* **2018**, *17*, 1027.

[15] a) D. Feng, T. Lei, M. R. Lukatskaya, J. Park, Z. Huang, M. Lee, L. Shaw, S. Chen, A. A. Yakovenko, A. Kulkarni, J. Xiao, K. Fredrickson, K. Fredrickson, J. B. Tok, X. Zou, Y. Cui, Z. Bao, *Nat. Energy* **2018**, *3*, 30; b) K. Wada, K. Sakaushi, S. Sasaki, H. Nishihara, *Angew. Chem., Int. Ed.* **2018**, *57*, 8886; c) R. Zhao, Z. Liang, R. Zou, Q. Xu, *Joule* **2018**, *2*, 2235.

[16] a) A. J. Clough, J. W. Yoo, M. H. Mecklenburg, S. C. Marinescu, *J. Am. Chem. Soc.* **2015**, *137*, 118; b) E. M. Miner, T. Fukushima, D. Sheberla, L. Sun, Y. Surendranath, M. Dincă, *Nat. Commun.* **2016**, *7*, 10942.

[17] a) M. G. Campbell, S. F. Liu, T. M. Swager, M. Dincă, *J. Am. Chem. Soc.* **2015**, *137*, 13780; b) S. Wang, J. Liu, H. Zhao, Z. Guo, H. Xing, Y. Gao, *Inorg. Chem.* **2018**, *57*, 541; c) M. Ko, A. Aykanat, M. K. Smith, K. A. Mirica, *Sensors* **2017**, *17*, 2192.

[18] a) K. Müllen, *Nat. Rev. Mater.* **2016**, *1*, 15013; b) J. Liu, C. Wöll, *Chem. Soc. Rev.* **2017**, *46*, 5730.

[19] D. Sheberla, L. Sun, M. Blood-Forsythe, S. Er, C. R. Wade, C. K. Brozek, A. Aspuru-Guzik, M. Dincă, *J. Am. Chem. Soc.* **2014**, *136*, 8859.

[20] a) B. Hoppe, K. D. J. Hindricks, D. P. Warwas, H. A. Schulze, A. Mohmeyer, T. J. Pinkvos, S. Zailskas, M. R. Krey, C. Belke, S. König, M. Fröba, R. J. Haug, P. Behrens, *CrystEngComm* **2018**, *20*, 6458; b) M. Hmadeh, Z. Lu, Z. Liu, F. Gándara, H. Furukawa, S. Wan, V. Augustyn, R. Chang, L. Liao, F. Zhou, E. Perre, V. Ozolins, K. Suenaga, X. Duan, B. Dunn, Y. Yamamto, O. Terasaki, O. M. Yaghi, *Chem. Mater.* **2012**, *24*, 3511.

[21] a) X. Fang, B. Zong, S. Mao, *Nano-Micro Lett.* **2018**, *10*, 64; b) G. Lu, O. K. Farha, W. Zhang, F. Huo, J. T. Hupp, *Adv. Mater.* **2012**, *24*, 3970.

[22] a) T. D. Bennett, A. K. Cheetham, *Acc. Chem. Res.* **2014**, *47*, 1555; b) T. D. Bennett, S. Horike, *Nat. Rev. Mater.* **2018**, *3*, 431; c) T. D. Bennett, A. L. Goodwin, M. T. Dove, D. A. Keen, M. G. Tucker, E. R. Barney, A. K. Soper, E. G. Bithell, J.-C. Tan, A. K. Cheetham, *Phys. Rev. Lett.* **2010**, *104*, 115503.

**ADVANCED
SCIENCE NEWS**

www.advancedsciencenews.com

**ADVANCED
ELECTRONIC
MATERIALS**

www.advelectronicmat.de

[23] a) M. Kalaj, K. C. Bentz, S. A. Jr., J. M. Palomba, K. S. Barcus, Y. Katayama, S. M. Cohen, *Chem. Rev.* **2020**, *120*, 8267; b) T. Tian, Z. Zeng, D. Vulpe, M. E. Casco, G. Divitini, P. A. Midgley, J. Silvestre-Albero, J.-C. Tan, P. Z. Moghadam, D. Fairen-Jimenez, *Nat. Mater.* **2018**, *17*, 174; c) W. Ling, G. Liew, Y. Li, Y. Hao, H. Pan, H. Wang, B. Ning, H. Xu, X. Huang, *Adv. Mater.* **2018**, *30*, 1800917; d) M. Wang, H. Shi, P. Zhang, Z. Liao, M. Wang, H. Zhong, F. Schwotzer, A. S. Nia, E. Zschech, S. Zhou, S. Kaskel, R. Dong, X. Feng, *Adv. Funct. Mater.* **2020**, *30*, 2002664.

[24] C. Liu, J. Wang, J. Wan, C. Yu, *Coord. Chem. Rev.* **2021**, *432*, 213743.

[25] a) R. Ameloot, F. Vermoortele, W. Vanhove, M. B. J. Roeffaers, B. F. Sels, D. E. D. Vos, *Nat. Chem.* **2011**, *3*, 382; b) X. Huang, P. Sheng, Z. Tu, F. Zhang, J. Wang, H. Geng, Y. Zou, C. Di, Y. Yi, Y. Sun, W. Xu, D. Zhu, *Nat. Commun.* **2015**, *6*, 7408; c) N. Lahiri, N. Lotfizadeh, R. Tsuchikawa, V. V. Deshpande, J. Louie, *J. Am. Chem. Soc.* **2017**, *139*, 19.

[26] V. Rubio-Giménez, M. Galbiati, J. Castells-Gil, N. Almora-Barrios, J. Navarro-Sánchez, G. Escorcia-Ariza, M. Mattera, T. Arnold, J. Rawle, S. Tatay, E. Coronado, C. Martí-Gastaldo, *Adv. Mater.* **2018**, *30*, 1704291.

[27] W.-H. Li, K. Ding, H.-R. Tian, M.-S. Yao, B. Nath, W.-H. Deng, Y. Wang, G. Xu, *Adv. Funct. Mater.* **2017**, *27*, 1702067.

[28] L. Hu, T. Xiong, R. Liu, Y. Hu, Y. Mao, M.-S. J. T. Balogun, Y. Tong, *Chem. - Eur. J.* **2019**, *25*, 6575.

[29] C. S. Grange, A. J. H. M. Meijer, M. D. Ward, *Dalton Trans.* **2010**, *39*, 200.

[30] a) K. Xiao, J. Tao, Z. Pan, A. A. Puretzky, I. N. Ivanov, S. J. Pennycook, D. B. Geohegan, *Angew. Chem.* **2007**, *119*, 2704; b) S. Pal, S. Maiti, U. N. Maiti, K. K. Chattopadhyay, *J. Mater. Chem. C* **2014**, *2*, 4005; c) M. Mahajan, S. K. Bhargava, A. P. O'Mullane, *RSC Adv.* **2013**, *3*, 4440.

[31] R. A. Heintz, H. Zhao, X. Ouyang, G. Grandinetti, J. Cowen, K. R. Dunbar, *Inorg. Chem.* **1999**, *38*, 144.

[32] a) D. Meng, J. L. Yang, C. Xiao, R. Wang, X. Xing, O. Kocak, G. Aydin, I. Yavuz, S. Nuryyeva, L. Zhang, G. Liu, Z. Li, S. Yuan, Z. Wang, W. Wei, Z. Wang, K. N. Houk, Y. Yang, *Proc. Natl. Acad. Sci. USA* **2020**, *117*, 20397; b) T.-H. Chen, I. Popov, W. Kaveevivitchai, Y.-C. Chuang, Y.-S. Chen, O. Daugulis, A. J. Jacobson, O. Š. Miljanić, *Nat. Commun.* **2014**, *5*, 5131.

[33] a) H. Topsoe, *Bulletin* **1968**, *472*, 63; b) F. M. Smits, *Bell Syst. Tech. J.* **1958**, *37*, 711; c) R. A. Weller, *Rev. Sci. Instrum.* **2001**, *72*, 3580.

[34] a) M. Ko, L. Mendecki, A. M. Eagleton, C. G. Durbin, R. M. Stolz, Z. Meng, K. A. Mirica, *J. Am. Chem. Soc.* **2020**, *142*, 11717; b) G. Skorupskii, B. A. Trump, T. W. Kasel, C. M. Brown, C. H. Hendon, M. Dincă, *Nat. Chem.* **2020**, *12*, 131.

[35] V. Rubio-Giménez, N. Almora-Barrios, G. Escorcia-Ariza, M. Galbiati, M. Sessolo, S. Tatay, C. Martí-Gastaldo, *Angew. Chem.* **2018**, *57*, 15306.